arXiv:2601.16096v3 [cs.NE] 24 Jun 2026

Neural Particle Automata: Learning Self-Organizing Particle Dynamics

HYUNSOO KIM*, KAIST, South Korea
EHSAN PAJOUHESHGAR*, EPFL, Switzerland
SABINE SÜSSTRUNK, EPFL, Switzerland
WENZEL JAKOB, EPFL, Switzerland
JINAH PARK, KAIST, South Korea

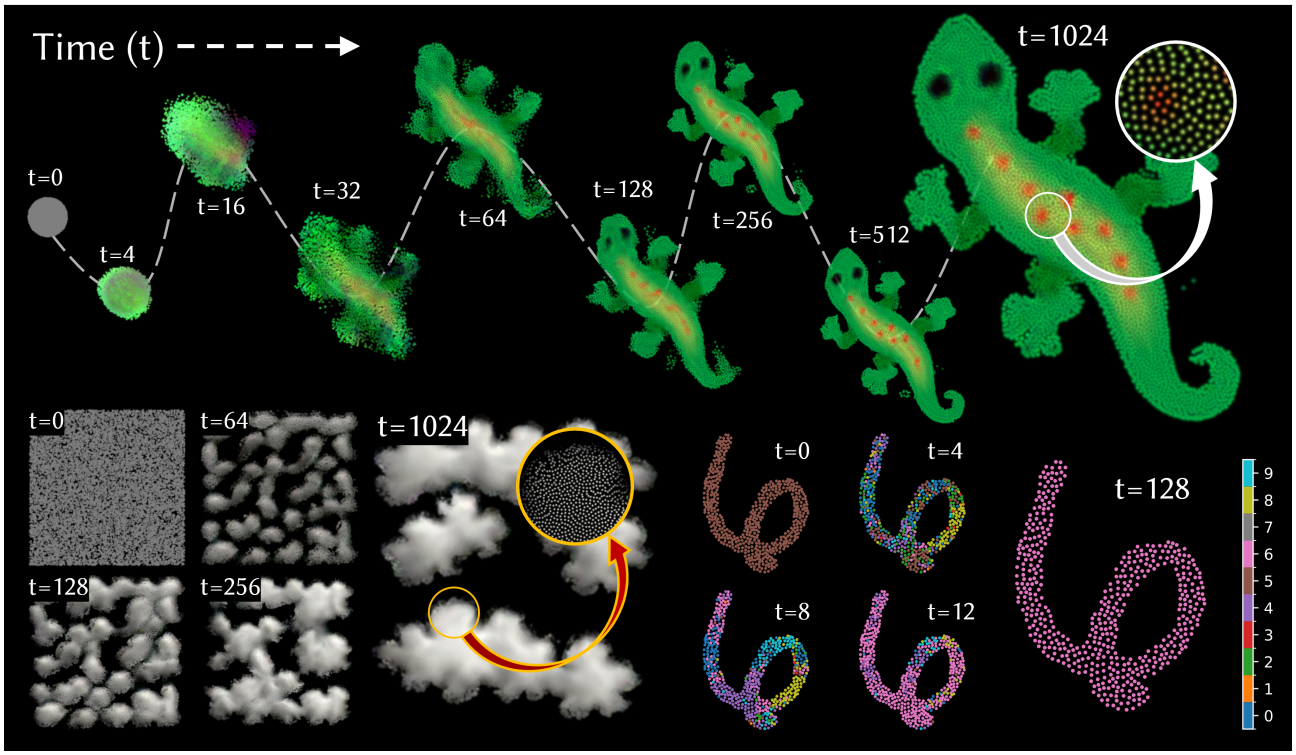


Fig. 1. **Neural Particle Automata** (NPA) are self-organizing particle dynamical systems driven by a shared, strictly local neural update rule. We show three distinct learned rules: (top) growing a morphology from an egg-like seed, (bottom left) RGBA texture formation from a uniform seed, and (bottom right) self-classifying particle digits; numbers denote time steps. Interactive web demo available at: **https://selforg-npa.github.io/**.

We introduce *Neural Particle Automata* (NPA), a Lagrangian generalization of Neural Cellular Automata (NCA) from static lattices to dynamic particle systems. Unlike classical Eulerian NCA where cells are fixed to pixels or voxels, NPA represent each cell as a particle with a continuous position and an internal state, both updated by a shared learnable neural rule. This particle-based formulation yields clear individuation of cells, allows heterogeneous dynamics, and focuses computation on regions where activity is present. However, particle systems introduce two challenges: neighborhoods are dynamic, and a naive implementation of local interactions scales quadratically with the number of particles. We address these issues by replacing grid-based perception with differentiable Smoothed Particle Hydrodynamics (SPH) operators, backed by memory-efficient CUDA kernels for scalable end-to-end training. Across tasks including morphogenesis, point-cloud classification, and particle-based texture synthesis, we show that NPA retain key NCA behaviors such as robustness and regeneration, while enabling new behaviors specific to particle systems. These results position NPA as a compact neural model for learning self-organizing particle systems.

*Both authors contributed equally to this research.

Authors' Contact Information: Hyunsoo Kim, KAIST, Daejeon, South Korea, khskhs@kaist.ac.kr; Ehsan Pajouheshgar, ehsan.pajouheshgar@epfl.ch, EPFL, Lausanne, Switzerland; Sabine Süsstrunk, sabine.susstrunk@epfl.ch, EPFL, Lausanne, Switzerland; Wenzel Jakob, wenzel.jakob@epfl.ch, EPFL, Lausanne, Switzerland; Jinah Park, KAIST, Daejeon, South Korea, jinahpark@kaist.ac.kr.

This work is licensed under a Creative Commons Attribution 4.0 International License.

CCS Concepts: • **Computing methodologies** → **Self-organization**; **Artificial life**; **Neural networks**; **Multi-agent systems**; **Point-based models**; *Real-time simulation*; *Interactive simulation*.

Additional Key Words and Phrases: Neural Cellular Automata, Self-Organization, Particle Systems

1 Introduction

Many natural phenomena exhibit self-organization: from magnetization in physical systems to morphogenesis and pigmentation in biology, and collective behaviors in bird flocks and ant colonies [Camazine et al. 2020]. In these systems, large numbers of simple entities interact only locally, yet collectively give rise to coherent global structure and behavior. Rather than being specified by their final appearance, these patterns emerge from local interactions and self-organize into a global configuration, as exemplified by reaction-diffusion systems [Turing 1952] and flocking models such as Boids [Reynolds 1987]. This self-organizing view offers distinct advantages over explicit, globally specified representations: it naturally extends to unbounded domains, generalizes across different resolutions and topologies due to its local nature, does not rely on global synchronization, and can progressively correct errors and recover from perturbations over time. These properties make self-organizing systems particularly attractive for interactive and real-time graphics applications.

Several computational models have been proposed to realize self-organizing representations and dynamics. Cellular automata [von Neumann 1966] are among the earliest such models, defined by discrete states and local interaction rules. Reaction-diffusion systems, originally introduced by Turing [1952], were later adapted to computer graphics for texture synthesis [Witkin and Kass 1991]. More recently, Model Synthesis [Merrell and Manocha 2010] and the Wave Function Collapse [Gumin 2016] have demonstrated self-organizing pattern generation in discrete domains.

Neural Cellular Automata (NCA) [Mordvintsev et al. 2020] take this idea further by replacing hand-crafted rules with neural networks: each cell has an internal state and repeatedly updates it based on local perception, with parameters learned from data or task objectives. Despite their simple update rule, they can produce robust and visually rich behaviors and have been successfully applied to tasks including texture synthesis [Niklasson et al. 2021; Pajouheshgar et al. 2024b], modeling growth [Mordvintsev et al. 2020; Pajouheshgar et al. 2025], and distributed classification [Kalkhof et al. 2023; Randazzo et al. 2020], establishing NCA as a compact and expressive framework for learning self-organizing dynamics.

Despite this progress, existing NCA models share a structural limitation: cells are pinned to a fixed lattice with static neighborhood relations. This Eulerian view leads to wasted computation in inactive regions and is poorly suited to heterogeneous dynamics, which requires cells to be treated as individual entities. Extensions of NCA to irregular domains such as graphs and meshes relax the regularity of the lattice but still assume fixed connectivity. In parallel, self-organizing systems such as Clusters [Ventrella 2016], Particle Life [Mohr 2022], and Particle-Lenia [Mordvintsev et al. 2022a] operate directly on particles with local interaction, but their dynamics are hand-designed and not trained from data. To the best of our knowledge, there is currently no framework that combines the robustness and expressivity of NCA with the unique advantages of particle-based systems.

In this work, we introduce *Neural Particle Automata* (NPA), a Lagrangian generalization of NCA from static lattices to dynamic particle systems. An NPA models each cell as a particle with a continuous position and an internal state, both updated by a shared, learnable rule. We obtain a particle-based analogue of NCA perception by replacing grid-based convolutions with mesh-free, differentiable Smoothed Particle Hydrodynamics (SPH) operators, which estimate densities, gradients, and other neighborhood features from nearby particles. These SPH-based features are then fed into a neural update rule that jointly adapts each particle's state and position, while preserving the strictly local, shared-rule structure of NCA. This structure makes NPA robust, lightweight[1], and well suited for real-time graphics applications. To make this practical at scale, we implement the SPH perception using memory-efficient, CUDA-accelerated kernels that avoid naive all-pairs interactions and dramatically improve training and inference speed as well as memory usage for large particle sets.

We evaluate NPA on a diverse set of tasks in 2D and 3D. First, we train NPA to self-organize from simple seeds into target morphologies, with particles dynamically rearranging to form the desired shapes. Second, we apply NPA to distributed classification of 2D and 3D point clouds, where local interactions between particles collectively give rise to a global prediction. Third, we use NPA for particle-based texture synthesis, where particles self-organize to match target textures. Across these settings, we show that NPA retain the robustness and regenerative behavior of NCA while exploiting the sparsity and flexibility of particle-based representations. The real-time interactive demo and the source code are available at: **https://selforg-npa.github.io/**.

2 Related Works

In this section, we provide background on NCA and discuss prior literature that motivates our approach of combining SPH operators with NCA architectures.

2.1 Neural Cellular Automata

NCA [Mordvintsev et al. 2020] are neural architectures inspired by classical cellular automata, in which an iterative local update rule is learned from data. This yields localized computation without global aggregation and iterative updates which do not rely on global synchronization. Despite the simplicity of this local non-linear rule, repeated application over time can give rise to complex global behavior.

Since their introduction, NCA have found applications in diverse tasks including texture synthesis [Larsson et al. 2025; Niklasson et al. 2021; Pajouheshgar et al. 2024b, 2023], modeling growth and morphogenesis [Mordvintsev et al. 2020; Pajouheshgar et al. 2025], and distributed classification and segmentation [Kalkhof et al. 2023; Randazzo et al. 2020]. Compared to conventional neural architectures, NCA offer several advantages: parameter efficiency through simple local rules; localized processing, which makes them hardware-friendly and enables spatial scalability; robustness to perturbations, and spatiotemporal generalization, as their updates can be interpreted as discretized partial differential equation (PDE) models [Pajouheshgar et al. 2024a], enabling inference under varied spatial and temporal step sizes. These properties make NCA well suited

[1] Parameterized by a neural network with as few as ten thousand parameters.

Table 1. Comparison of spatial operators based on desired properties. **U**: Does it work on unstructured data? **S**: Does it exploit the spatial structure in data? **DY**: Can it be effectively applied to dynamic data? **LO**: Is the influence of single operation local? **SC**: Is it scalable with increasing data resolution? **UR**: Does it generalize over unseen resolutions/samplings?

Spatial Operators	U	S	DY	LO	SC	UR
Convolutions	✗	✔	✗	✔	✔	✗
Graph convolutions	✗	✔	✔	✔	✔	✗
Set operators	✔	✗	✔	✗	✔	✗
Attention mechanism	✔	✗	✔	✗	✗	✗
Mesh differentials	✗	✔	✗	✔	✔	✔
SPH operators	✔	✔	✔	✔	✔	✔

for interactive and real-time graphics scenarios where compactness, locality, and robustness are desirable.

A key feature of NCA is the decoupling between the learnable update rule and the spatial perception operator. Early work used fixed Sobel and Laplacian filters on regular grids [Mordvintsev et al. 2020; Niklasson et al. 2021], while later variants replaced these with operators defined on graphs [Grattarola et al. 2021], meshes [Pajouheshgar et al. 2024b], and other irregular discretizations [Kim and Park 2025; Mordvintsev et al. 2022b, 2021; Niklasson et al. 2021]. This modularity allows the same local update rule to be reused across different domains by changing only the perception operator, enabling generalization across meshes [Pajouheshgar et al. 2024b], from quadrilateral grids to Voronoi and hexagonal grids [Mordvintsev et al. 2022b; Niklasson et al. 2021], and from 2D to 3D domains [Kim and Park 2025; Mordvintsev et al. 2021]. This perspective highlights the central role of the spatial operator in neural networks, which we review in the following section.

2.2 Spatial Operators in Neural Networks

A *spatial operator* in a neural network is any mechanism that propagates information across space by aggregating features over regions of the domain (e.g. pixels, vertices, points), before passing them to subsequent layers. In NCA, this corresponds to the perception stage where a cell gathers information from its neighbors before applying the neural update rule. A wide variety of spatial operators have been proposed across architectures; Table 1 summarizes representative examples. These families differ in the domains they support, their degree of locality and scalability, and how well they generalize across resolutions or samplings.

Convolution is one of the most common operators for processing images or data on regular grids. A large body of work extends convolution to point sets by combining learned kernels with explicit neighborhood queries [Li et al. 2018; Thomas et al. 2019; Wu et al. 2019]. While both point-based convolutions and NPA require neighborhood queries, the role of the neighborhood operator differs: point convolutions *learn* the spatial kernel (and often its aggregation behavior) which can be sensitive to particle positions in the neighborhood, whereas NPA uses fixed SPH operations as sampling-robust perception mechanism.

Graph Neural Networks (GNNs) offer an alternative based on graph message passing [Grattarola et al. 2021], making them natural for data with explicit connectivity such as meshes or skeletons. However, standard message passing is topology-first and often more sensitive to the graph structure than to the underlying geometry. Geometry-aware and mesh-specific extensions partly address this issue [Hanocka et al. 2019; Liu et al. 2023], but they still rely on explicit, typically static connectivity, making them ill-suited for handling dynamic systems where neighborhoods change over time.

Set-based operators treat inputs as unordered point sets and aggregate features in a permutation-invariant way. PointNet [Qi et al. 2017a] employs such global set operators for spatial communication, with PointNet++ [Qi et al. 2017b] adding hierarchical pooling to recover some notion of locality, but permutation invariance still makes it difficult to capture oriented local geometry. Attention mechanisms [Vaswani et al. 2017] provide a more expressive global operator by learning pairwise weights via key-query matching, and have been adapted to point clouds and other spatial domains [Zhao et al. 2021]. However, global attention is computationally expensive for high-resolution spatial data and typically relies on downsampling or windowing, while local attention variants tend to lose long-range interactions and require additional positional encodings to represent geometry faithfully.

Differential operators on meshes have recently been used as spatial operators in neural networks, with promising robustness to discretization. DiffusionNet [Sharp et al. 2022] uses heat diffusion on manifolds, DeltaConv [Wiersma et al. 2022] applies gradient and divergence operators to scalar/vector features, and PoissonNet [Maesumi et al. 2025] incorporates a Poisson solver to give each layer global spatial support. These methods generalize well across discretizations because differential operators are robust to mesh tessellation, allowing networks to learn continuous representations rather than grid-specific features. However, they still rely on connectivity to define the operators, which limits their applicability to particle-based systems.

Smoothed Particle Hydrodynamics (SPH) [Gingold and Monaghan 1977; Lucy 1977] provides a mesh-free way to approximate differential operators via kernel-weighted sums over neighboring particles. Compared to other mesh-free schemes such as GMLS [Mirzaei et al. 2012], SPH avoids matrix inversion, which simplifies implementation and improves numerical stability. See Koschier et al. [2022] for a comprehensive overview on SPH methods. Previous work that combines SPH with neural networks uses SPH within differentiable simulators, mainly for fluid modeling and control [Schenck and Fox 2018; Toshev et al. 2024; Winchenbach and Thuerey 2025]. In contrast, NPA employ SPH as a mesh-free perception operator within an NCA-style iterative local update rule, enabling diverse self-organizing behaviors beyond fluid dynamics.

SPH is a radial basis function (RBF) approach to mesh-free numerical method for PDEs. RBF interpolation has been used with neural network as RBF networks [Broomhead and Lowe 1988], later used in deep learning [Hryniowski and Wong 2019] and neural field representation [Chen et al. 2023]. However, RBF networks utilize RBF interpolation only for point-wise nonlinearity, while NPA use SPH method for spatial message passing between nodes, allowing deeper understanding of spatial relations in data.

3 Method

NCA operate on a set of cells, each with an internal state $\mathbf{S}_i$ and a fixed position $\mathbf{x}_i$. In classical NCA, $\mathbf{x}_i$ are fixed to a lattice and the neighborhood structure is given implicitly by the lattice, so perception is implemented with grid operators such as convolutions. In this work, we incorporate particle-based perception with differentiable SPH operators, which provide mesh-free estimates of local neighborhood features, preserving the strictly local, shared-rule structure of NCA while extending NCA on unstructured particles.

3.1 Differentiable SPH Operators

Smoothed Particle Hydrodynamics (SPH) is a mesh-free numerical method that represents continuous fields with discrete particles and evaluates field quantities via kernel-weighted sums over nearby samples within a **support radius** ϵ. This kernel-weighted interpolation provides direct, local estimates of differential operators from particles without explicit connectivity.

3.1.1 Mathematical Formulation for SPH Methods. We denote the inputs as a set of point samples ($\mathbf{x}_i \in \mathbb{R}^D, m_i \in \mathbb{R}, \mathbf{S}_i \in \mathbb{R}^C$), where each tuple represents the position in D-dimensional space, the mass, and the sampled value of a C-dimensional field for particle i, respectively. SPH is parameterized by a support radius $\epsilon \in \mathbb{R}$ and kernel functions $W_\epsilon : \mathbb{R}^D \to \mathbb{R}$ and $W_\epsilon^\nabla : \mathbb{R}^D \to \mathbb{R}^D$, which take $\mathbf{r}_{ji} = \mathbf{x}_j - \mathbf{x}_i$ as input and return scalar weight or vector weight gradient, respectively. Table 2 summarizes the SPH operators used in our differentiable framework. We use the Poly6 kernel W_ϵ for smoothing and Spiky kernel W_ϵ^∇ for gradient, which are defined in 2D space as:

$$\begin{aligned} W_\epsilon(\mathbf{r}) &= \frac{4}{\pi\epsilon^8}\left(\epsilon^2 - \|\mathbf{r}\|^2\right)^3, \qquad 0 \le \|\mathbf{r}\| \le \epsilon, \\ W_\epsilon^\nabla(\mathbf{r}) &= \frac{10}{\pi\epsilon^5}\left(\epsilon - \|\mathbf{r}\|\right)^2 \frac{\mathbf{r}}{\|\mathbf{r}\|}, \quad 0 < \|\mathbf{r}\| \le \epsilon. \end{aligned} \tag{1}$$

Using spiked kernels such as W_ϵ^∇, rather than ∇W_ϵ, may not preserve momentum and entropy in high-accuracy simulations [Dehnen and Aly 2012]. However, it has demonstrated better numerical stability with plausible realism in interactive applications [Müller et al. 2003], which our use of SPH operators is more aligned with. Especially, W_ϵ^∇ always gives greater magnitude of gradients as $\mathbf{r} \to 0$, which is an expected behavior as particles get closer.

Table 2. SPH operators used in NPA and their output dimension.

Operator	Formula	Dim.
Density	$\rho_i = \sum_j m_j W_\epsilon(\mathbf{r}_{ji})$	1
Smoothing	$\tilde{\mathbf{S}}_i = \sum_j \frac{m_j}{\rho_j}\mathbf{S}_j W_\epsilon(\mathbf{r}_{ji})$	C
Density gradient	$\nabla\rho_i = \sum_j m_j W_\epsilon^\nabla(\mathbf{r}_{ji})$	D
Moment Matrix	$\mathbf{M}_i = \sum_j \frac{m_j}{\rho_j}\mathbf{r}_{ji}\, W_\epsilon^\nabla(\mathbf{r}_{ji})^T$	$D \times D$
Gradient, 0-th order (difference formula)	$\nabla_0\mathbf{S}_i = \sum_j \frac{m_j}{\rho_j}(\mathbf{S}_j - \mathbf{S}_i)\, W_\epsilon^\nabla(\mathbf{r}_{ji})$	$C \times D$
Gradient, 1-st order [Bonet and Lok 1999]	$\nabla_1\mathbf{S}_i = \mathbf{M}_i^{-1}\nabla_0\mathbf{S}_i$	$C \times D$

3.1.2 Backward Formulation. We analytically derive the backward formula for each SPH operator to enable end-to-end differentiable optimization. For example, the gradient of the loss $\mathcal{L}(\tilde{\mathbf{S}})$ with respect to a single channel sampled value S_i is written as

$$\frac{\partial\mathcal{L}}{\partial S_i} = \sum_j \frac{\partial\mathcal{L}}{\partial\tilde{S}_j}\frac{\partial\tilde{S}_j}{\partial S_i} = \sum_j \frac{\partial\mathcal{L}}{\partial\tilde{S}_j}\frac{m_i}{\rho_i}W_\epsilon(\mathbf{r}_{ij}). \tag{2}$$

Note the backward formulation has the same neighborhood aggregation structure as the forward formulations in Table 2. Thus, the backward pass can be implemented within the same computational framework as the forward pass, without additional intermediate arrays. See Appendix for backward formulations of other operators.

The 0th-order SPH gradient $\nabla_0\mathbf{S}_i$ (Table 2) is a simple difference-based estimator that can be biased under irregular sampling. The 1st-order variant corrects this bias using the *moment matrix* $\mathbf{M}_i$, which summarizes the local neighbor geometry and serves as a normalization that makes the estimate exact for locally linear fields: $\nabla_1\mathbf{S}_i = \mathbf{M}_i^{-1}\nabla_0\mathbf{S}_i$. In practice, however, differentiating through $\mathbf{M}_i^{-1}$ can be unstable and costly, so we use the following alternative,

$$\nabla\mathbf{S}_i \;=\; \nabla_0\mathbf{S}_i \;+\; \Big(\nabla_1\mathbf{S}_i - \nabla_0\mathbf{S}_i\Big).\texttt{detach()}, \tag{3}$$

which uses the corrected gradient for the forward pass while backpropagating as if ∇_0 were used. This removes backpropagation through $\mathbf{M}_i^{-1}$ and improves training stability; when $\det(\mathbf{M}_i) < 10^{-3}$, we skip the correction and fall back to ∇_0.

3.1.3 CUDA Implementation. For dynamic particle systems, neighborhoods change over time, and expressing the resulting neighborhood aggregation in connectivity matrices can lead to large, inefficient computational graphs and significant overhead. We implement mesh-free SPH perception using custom differentiable CUDA kernels with hash-grid acceleration to make training and inference scalable in both runtime and memory. In contrast to differentiable SPH toolkits targeting inverse problems in fluid dynamics (e.g., JAX-SPH [Toshev et al. 2024], DiffSPH [Winchenbach and Thuerey 2025]), our operators target a general-purpose feature processing for neural networks. Thus, we designed our operators with batch processing and arbitrary feature dimensionality in mind.

We bin particles into a uniform hash-grid with cell size equal to the support radius ϵ, and apply a permutation to obtain a *cell-contiguous* memory layout, similar to Goswami et al. [2010]. SPH operators then scan the 3^D adjacent cells and apply the true radius test before accumulating contributions. To balance simplicity and performance, we provide two forward kernels: (i) a vanilla thread-per-particle implementation that uses Morton hashing to improve cache locality, and (ii) a more optimized kernel that utilizes shared-memory by assigning thread blocks to grid cells (splitting crowded cells when needed) where threads cooperatively read and write consecutive neighbor-cell spans into shared memory in fixed-size strides, enabling coalesced global loads and reuse across particles in the block. See Appendix for detailed CUDA implementation.

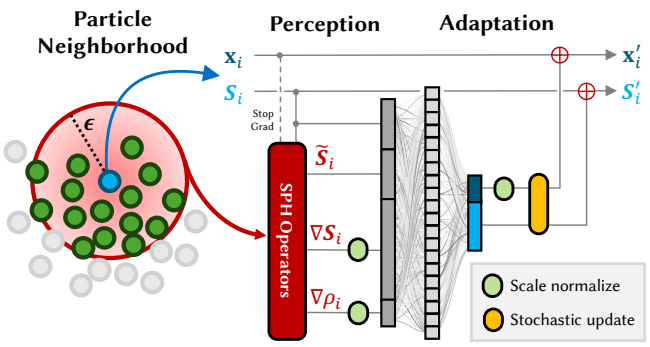


Fig. 2. Single update step of Neural Particle Automata.

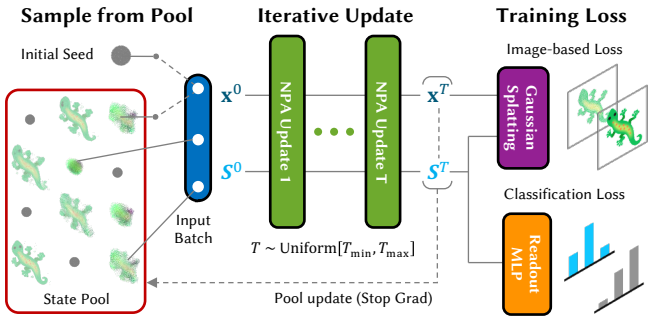


Fig. 3. Training of Neural Particle Automata.

3.2 Neural Particle Automata

We propose *Neural Particle Automata*, which combines SPH-based, mesh-free perception with the local, shared-rule structure of NCAs. Each particle computes a compact perception vector from nearby particles via SPH operators, and a small shared MLP maps this vector to state updates (and optional position updates). We describe the update rules for static and dynamic particles and summarize practical techniques that stabilize training.

3.2.1 NPA update rule. At each step, every particle i forms a perception vector from its ϵ-neighborhood using SPH operators,

$$\mathbf{Z}_i = \left[\mathrm{S}_i,\ \tilde{\mathrm{S}}_i,\ \nabla \mathrm{S}_i,\ \nabla \rho_i\right], \tag{4}$$

and applies a shared adaptation network f_θ to predict an update. We use a similar update scheme for both static and dynamic particle sets. Given the perception vector $\mathbf{Z}_i$, the adaptation network f_θ, which consists of a two-layer MLP with a ReLU activation, predicts an increment

$$\Delta \mathbf{y}_i = f_\theta(\mathbf{Z}_i) = \mathbf{W}_2(\mathbf{W}_1 \mathbf{Z}_i + \mathbf{b}_1)_+, \tag{5}$$

where $\Delta \mathbf{y}_i = \Delta \mathrm{S}_i$ for *static* particles and $\Delta \mathbf{y}_i = [\Delta \mathbf{x}_i; \Delta \mathrm{S}_i]$ for *dynamic* particles. Each iteration of the NPA update rules, as shown in Figure 2 applies an additive increment to the state (and position if needed), analogous to a single forward-Euler integration step:

$$\mathrm{S}_i \leftarrow \mathrm{S}_i + \delta\, \Delta \mathrm{S}_i, \tag{6}$$

$$\mathbf{x}_i \leftarrow \mathbf{x}_i + \delta\, \Delta \mathbf{x}_i. \tag{7}$$

We use a stochastic update mask $\delta \sim \text{Bernoulli}(p)$ with update probability $p = 0.5$ following Mordvintsev et al. [2020]. The mask updates a random subset of particles per step, reducing reliance on global synchronization. We study test-time behavior under different values of p in § 4.4.

Perception produces a compact set of local features: the particle's own state S_i together with neighborhood summaries $\tilde{\mathrm{S}}_i$ and $\nabla \mathrm{S}_i$, which can be interpreted as value- and derivative-like measurements of the underlying field. In particular, $(\mathrm{S}_i - \tilde{\mathrm{S}}_i)$ carries diffusion/Laplacian-like information (roughly $(\mathrm{S}_i - \tilde{\mathrm{S}}_i) \propto \epsilon^2 \Delta \mathrm{S}_i$), so while SPH formulations for Laplacian exist, we do not use an explicit SPH Laplacian in perception. We additionally include the density gradient $\nabla \rho_i$ as a geometric cue specific to particle discretizations, where sampling density can vary across space and time. Because $\tilde{\mathrm{S}}$ and $\nabla \mathrm{S}$ are normalized to be density-insensitive, $\nabla \rho$ provides the missing signal of local crowding and sparsity, and directional information about where density increases or decreases.

3.2.2 Equivariance of NPA. SPH-based perception is inherently invariant to permutations of particle indices and to global translations by construction. We additionally design NPA to be equivariant to changes in sampling density and spatial scale, so the same learned rule can be applied under different particle counts and spatial length scales. While we do not enforce rotational equivariance in this work, it can also be incorporated, for instance by using Vector Neurons [Deng et al. 2021] for gradient inputs in the adaptation stage.

To generalize across different sampling densities—i.e., using more or fewer particles while keeping the support radius ϵ fixed—we normalize particle masses so that the total mass remains constant (set to 1). Concretely, if the particle count increases by a factor k, we scale each particle mass by $1/k$, which keeps the magnitude of $\nabla \rho$ consistent. Note that $\tilde{\mathrm{S}}$ and $\nabla \mathrm{S}$ are designed to be invariant to particle count as they are normalized by ρ by definition.

Uniformly scaling space and the support radius as $(\mathbf{x}, \epsilon) \mapsto (c\mathbf{x}, c\epsilon)$ represents the same configuration at a different scale and should induce consistent behavior (up to rescaling). Under this transformation, the scale-dependent inputs are scaled: $\nabla \mathrm{S}$ by $1/c$, and $\nabla \rho$ by $1/c^{D+1}$. For dynamic particles, we scale the displacement $\Delta \mathbf{x}$ by ϵ for the network to learn scale-independent motion.

3.2.3 Training NPA. Figure 3 summarizes our training pipeline. In addition to standard NCA practices—sampling a variable number of update steps, training with a state pool for persistence, and using an overflow regularizer to keep S within $[-1, 1]$—we introduce several techniques to stabilize the NPA training.

Vector-valued perception terms (e.g., $\nabla \mathrm{S}$ and $\nabla \rho$) can occasionally have very large magnitudes and destabilize training. Inspired by logarithmic response curves in biological sensory systems, we scale each vector $\mathbf{v}$ as

$$\mathbf{v} \leftarrow \log(1 + |\mathbf{v}|)\, \frac{\mathbf{v}}{|\mathbf{v}| + \eta}, \tag{8}$$

where $\eta > 0$ is a small constant for numerical stability.

For dynamic particles, we stop gradients with respect to positions in the SPH perception, as shown in Figure 2. Empirically, this improves stability and convergence and enables larger learning rates. To discourage sporadic motion, we regularize the total displacement

over rollout steps, $\sum_t \|\Delta \mathbf{x}^{(t)}\|$, encouraging smooth, consistent trajectories. For image-supervised tasks, we decode per-particle states into renderable attributes and rasterize them with Gaussian splatting to obtain color and density maps. Task-specific losses are then applied on these rendered outputs; we provide more details on the decoding and losses for each task in the following section.

4 Experiments

We evaluate NPA on three representative tasks that highlight different aspects of learned self-organization: (i) **morphogenesis**, where a dynamic particle set self-organizes from a simple seed into a target shape in 2D and 3D; (ii) **particle-based texture synthesis**, where dynamic particles form stochastic texture patterns; and (iii) **point-cloud classification**, where a static point set performs distributed classification via iterative local communication. We also conduct a set of analyses to illustrate characteristic test-time properties of our NPA model. Our configuration is shown in Table 3. See Appendix for ablation studies on the architecture and the hyperparameters. **All figures are best viewed digitally when zoomed in.**

4.1 Morphogenesis Modeling

Morphogenesis highlights the ability of NPA to self-organize complex structure from a simple, unstructured initial configuration. We initialize particles uniformly inside a ball with zero state—an "egg-like" setting in which all matter is present from the start and must be reorganized into the target form—and evolve them using a shared, trainable local rule. Training supervises only the *rendered outcome*, allowing particles to freely rearrange as long as the rendered result matches the target. As a result, NPA acts as an implicit, dynamical representation of morphologies: global structure emerges through repeated local interactions rather than from an explicit parameterization or particle-to-target correspondence.

4.1.1 2D Shapes. We train NPA to grow colored 2D shapes from a simple seed on a dataset of 60 emoji targets. To define image-space supervision without correspondences, we first convert each target emoji into a colored point set by sampling roughly 4096 points from the target image. We then render both the generated particle set and the target point set onto a fixed grid using isotropic Gaussian splatting, producing a color image and a density map for each.

Table 3. Training and model configuration for all experiments.

	Setting	Growing 2D Morphology	Growing 3D Morphology	Particle Textures	Point-Cloud Classification
NPA	#Particles (N)	4096	16384	4096	512
	SPH radius (ϵ)	0.1	0.1	0.2	0.1
	Seed	Uniform ball (radius 0.2)	Uniform ball (radius 1.0)	Uniform square (side length 2.0)	PointMNIST
	Channels (C)	16	24	16	16
	MLP width	128	256	128	256
	#Parameters	11k	38k	11k	21k + 7k
Training	$[T_{\min}, T_{\max}]$	[32, 96]	[24, 48]	[16, 32]	[12, 24]
	Batch size	8	4	8	64
	Iterations	30k	20k	12k	50k
	Learning rate	0.0005	0.003	0.0001	0.001
	Weight decay	0	0	0.1	0.1
	Pool size	512	16	512	1024

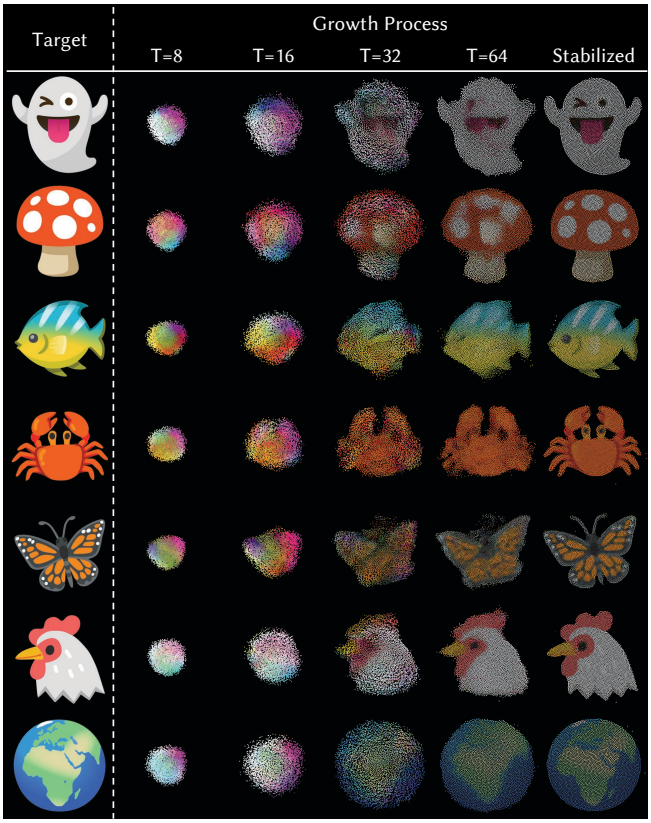


Fig. 4. **Growing 2D Morphology** Starting from the same egg-like seed, learned NPA rules self-organize into different emoji targets.

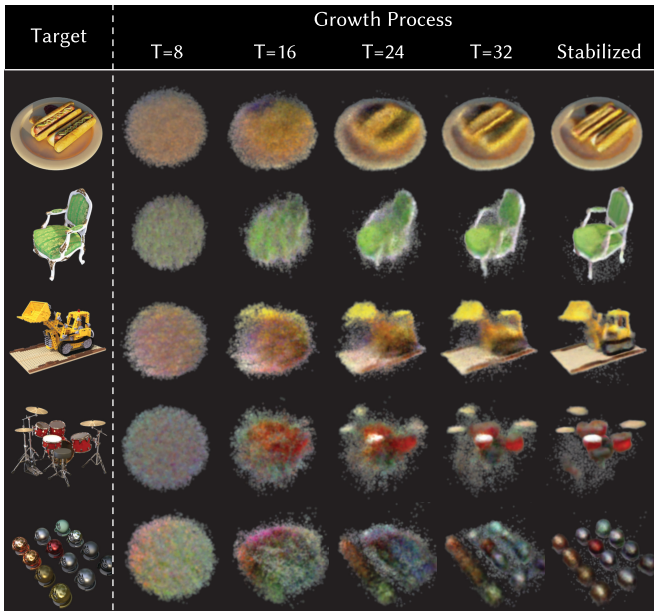


Fig. 5. **Growing 3D Morphology** A learned NPA rule grows a gaussian-splat representation from a compact seed under 3D multi-view supervision.

Particle color is obtained from the last three state channels. We supervise both geometry and appearance using losses on the rendered density and color maps. To encourage stable training, we weight the color loss by a detached function of the density error so that the model first prioritizes placing mass correctly (learning shape) before refining color. Concretely, letting D, C denote the rendered density and color, and $D^\star, C^\star$ their targets, we use a $\ell_1 + \ell_2$ loss for density $\mathcal{L}_{\text{dens}}(D, D^\star)$ and color $\mathcal{L}_{\text{col}}(C, C^\star)$, with the color term down-weighted in regions of large density mismatch (with the weight detached). Qualitative results for 2D morphogenesis are shown in Figure 4. Compared to grid-based GrowingNCA [Mordvintsev et al. 2020], our particle-based NPA is more memory efficient for the same details while taking more time. See Appendix for quantitative comparisons.

4.1.2 3D Objects. We additionally train NPA to self-organize into 3D objects under multi-view supervision, in the spirit of 3D Gaussian splatting. Each particle's position and states $(\mathbf{x}_i, \mathbf{S}_i)$ is converted into Gaussian parameters $(\mu_i, \mathbf{c}_i, \mathbf{q}_i, \sigma_i, o_i)$ as follows:

$$
\begin{aligned}
\mu_i &= \mathbf{x}_i, && \text{(Position)}\\
\mathbf{c}_i &= \mathbf{S}_i[12{:}24], && \text{(View-dependent color)}\\
\mathbf{q}_i &= \texttt{normalize}(\mathbf{S}_i[8{:}12]), && \text{(Rotation)}\\
\mathbf{A}_i &= A\tanh(\mathbf{S}_i[4{:}8]/A), && \text{(Anisotropy)}\\
\sigma_i &= \sigma\exp(\mathbf{A}_i[0{:}3]), && \text{(Scale)}\\
o_i &= o\exp(\mathbf{A}_i[3]), && \text{(Opacity)}
\end{aligned}
$$

where A, σ, o represent the maximum anisotropy, default scale, and default opacity, respectively. $A = 0.1, \sigma = 0.02, o = 0.15$ are used for the experiments. Gaussians are rendered into color and alpha images using GSplat [Ye et al. 2025], and then multi-scale SSIM is used as a photometric loss between rendered and target views. In addition to the photometric loss, we penalize anisotropic outliers with an isotropy regularizer $\mathcal{L}_{iso} = \frac{1}{N}\sum_i ||A_i||_1$.

To improve foreground/background separation, we render with a white noise background during training. We also employ a coarse-to-fine curriculum by initially starting with blurred target image and gradually reducing the blurring radius, allowing the model to first capture coarse structure before refining fine details. Figure 5 shows the evolution of 3D morphogenesis trained on the NeRF synthetic dataset [Mildenhall et al. 2021].

4.2 Particle-based Texture Synthesis

We next evaluate NPA on particle-based texture synthesis, shown in Figure 6, where the goal is to generate a target *RGBA* texture with transparency by self-organizing a dynamic particle set from a uniform square initialization. Given particle positions and states, we use the first three channels of the state as the particle's color and render the particle set to a grid using Gaussian splatting, producing an RGB color map $\mathbf{C}$ and a scalar density map D. To define a target for supervision, we convert the RGBA texture into a point set by sampling approximately the same number of points from the target and splatting them in the same way, yielding target maps $\mathbf{C}^\star$ and $D^\star$. Supervising both density and color allows particles to jointly match *where* texture content appears (alpha) and *what* it looks like (RGB).

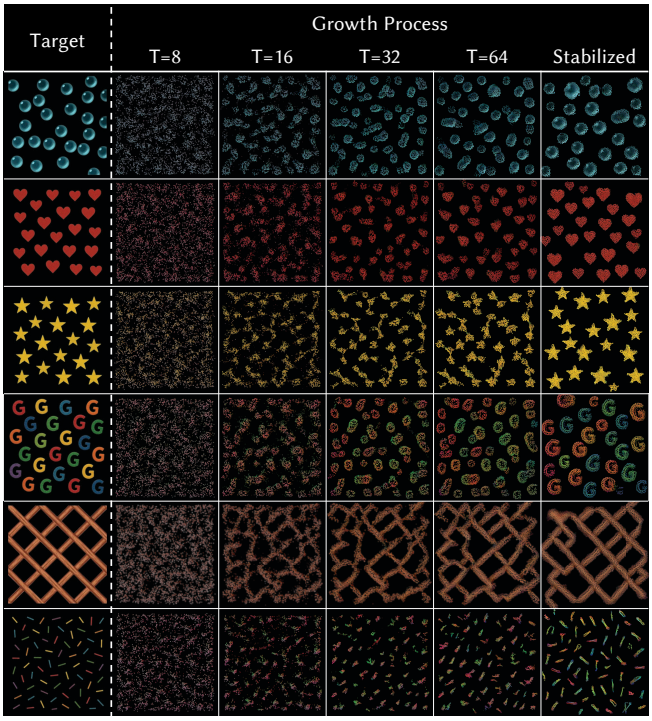


Fig. 6. **Particle-based Texture Synthesis.** From a uniform square seed, a learned NPA rule self-organizes dynamic particles into textures.

To compare rendered outputs with targets, we use the VGG-feature optimal-transport texture loss from Kolkin et al. [2019] as adopted in Pajouheshgar et al. [2023]. This loss compares multi-scale feature distributions (rather than enforcing pixel-wise alignment), which is well-suited for texture synthesis. Since VGG features are defined on RGB images [Simonyan and Zisserman 2015] but our rendering produces four channels, we apply the texture loss *separately* to the color map and the density map: we feed $\mathbf{C}$ directly, and we repeat the density map across channels so that D can be treated as a three-channel image.

Exact density values are often less important than the *support* of the density (whether particles occupy the right regions), so we apply a soft power transform $\bar{D} = (D + \eta)^\alpha$, (and likewise with the target density $\bar{D^\star}$) where $\alpha = 0.1$ and $\eta = 10^{-6}$ is a small constant to ensure numerical stability. This reduces sensitivity to absolute density magnitudes and empirically improves visual quality by encouraging the model to first establish the correct spatial occupancy before refining appearance.

4.3 Self-classifying point clouds

We evaluate NPA on point cloud classification tasks to study whether global semantic decisions can emerge from purely local particle interactions. We create a PointMNIST dataset by sampling 512 uniform points from each MNIST image, in range $[0, 1]^2$. We first upsample the image to 224^2, and randomly sample a point from each pixel with value greater than 0.5. The number of points is then reduced to 512 using farthest point sampling.



Fig. 7. **Self-classifying MNIST Points.** A static point set representing MNIST digits iteratively exchanges local information until reaching a global consensus for classification.

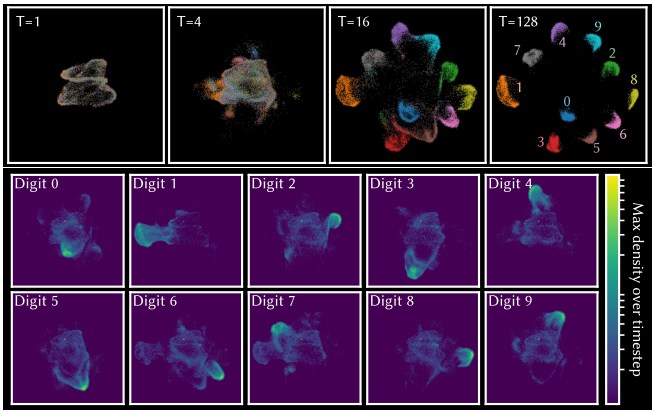


Fig. 8. Internal state visualization of self-classifying Point MNIST. (Top) Evolution of internal states by digits on reduced 2D space. (Bottom) Maximum density of internal states over the total timesteps by each digit.

Following Randazzo et al. [2020], we replace the cross entropy loss with an L_2 loss on the one-hot target vectors. Empirically this stabilizes the long-term dynamics by preventing blow-ups. Our architecture achieved 98.42% classification accuracy on the test set. Figure 7 illustrates the evolution of correctly classified examples for each digit, where every particle reaches consensus using only local operations. Figure 8 shows the internal state evolution of 200 digits after dimension reduction with UMAP [McInnes et al. 2018] and the *footprint* of internal states for each digit on the reduced space. The iterative nature of NPA lets us visualize how NPA understands the shape of digits and forms a global consensus in detail.

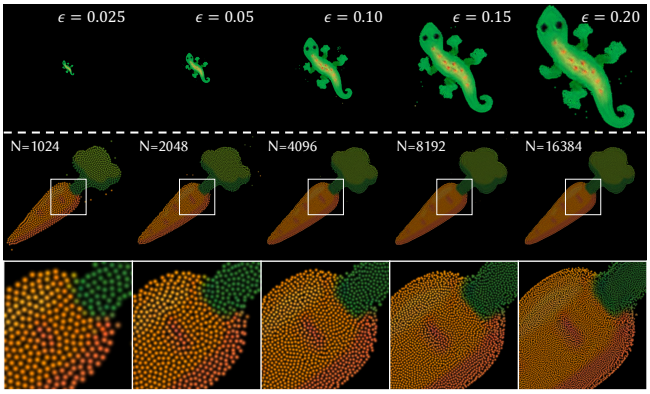


Fig. 9. **Robustness to Discretizations.** Varying ϵ and N at test time.

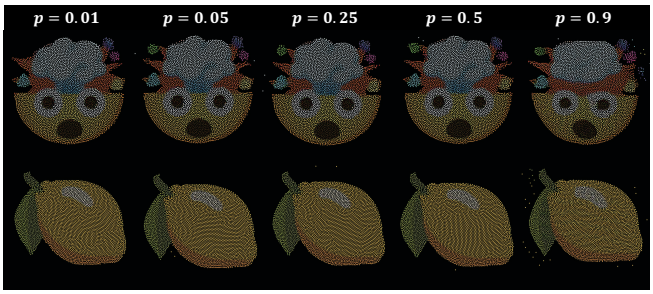


Fig. 10. NPA remains stable for different stochastic update probabilities p.

4.4 NPA Properties

NPA models have several interesting test-time properties. Figure 9 probes robustness to discretization by varying the SPH support radius ϵ and the number of particles N at inference time for a model trained with (N=4096, ϵ=0.1). When changing ϵ, we rescale the initial seed accordingly; by design, this preserves the NPA dynamics up to numerical precision (i.e., float round-off), and we observe stable behavior across a broad range of ϵ. When changing N, we do not have a formal equivariance guarantee, but empirically the dynamics degrade gracefully at lower particle counts and typically improve as N increases, where SPH neighborhood estimates become more accurate. Zoomed-in views highlight how sampling density affects local coverage and particle spacing. Additionally, Figure 10 shows that NPA is robust to varying the update probability p at inference time, despite all models being trained with $p = 0.5$. In the limit $p \to 0$, the stochastic updates approach a Poisson process, yielding effectively asynchronous dynamics with no global synchronization.

Figure 11 illustrates the regenerative behavior of NPA under three types of perturbations: (i) locally zeroing particle states, (ii) cut-like disruptions, and (iii) clumping particles by pulling them

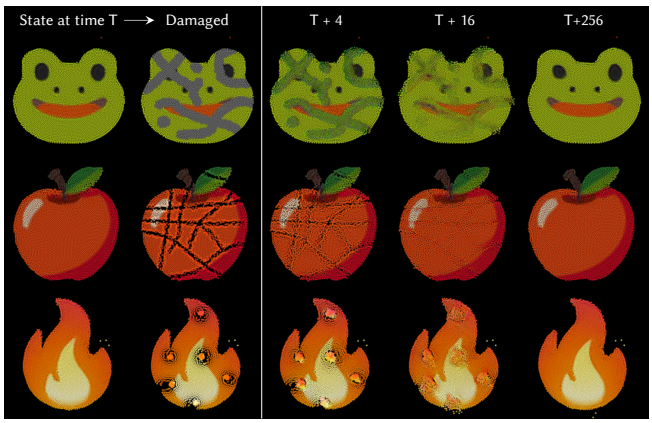


Fig. 11. **Regeneration.** Continued application of the learned local rule repairs damage and recovers from state erasure, cuts, and clumping.

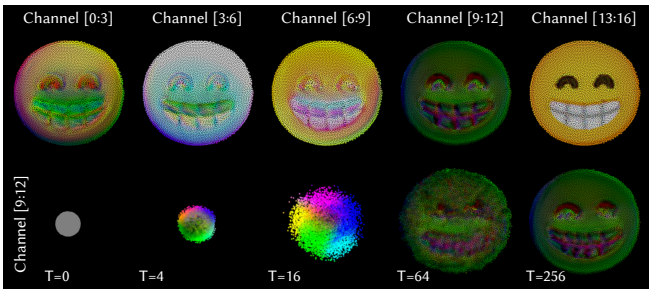


Fig. 12. **Hidden Channels.** Internal states form a spatially structured representation, guiding the growth and helping with long-term stability.

toward a point. In all cases, continued application of the learned local rule repairs the damage and recovers the target structure. To encourage such regeneration in the 2D morphogenesis and texture settings, we apply a simple training-time disturbance: whenever we sample an element from the pool, we pick a random particle and set the states of all particles within its ϵ-neighborhood to zero. This local perturbation regularizes the dynamics toward self-correction; notably, the other two distortions are never seen during training, yet the resulting models still recover from them at test time.

To better understand what the learned rule encodes, Figure 12 visualizes the hidden state channels by rendering channel groups as RGB. The channels consistently organize into spatially meaningful patterns, suggesting that they act as internal representations that help particles infer their role within the emerging morphology. In particular, channels [9:12] often exhibit a rainbow-like structure during early stages of growth, consistent with a directional signal that guides differentiation and expansion from the seed. We also observe that, even after the target shape is reached, particles typically continue moving within the object, forming vortex-like trajectories as shown in Figure 13. Because the image-based objective does not enforce particle correspondences, such persistent flows naturally emerge as stable solutions of the learned dynamics. We speculate



Fig. 13. **Persistent Internal Flows.** Even after the target is reached, particles typically keep moving within the shape; the resulting vortex-like vector field indicates stable circulating trajectories under the learned dynamics.

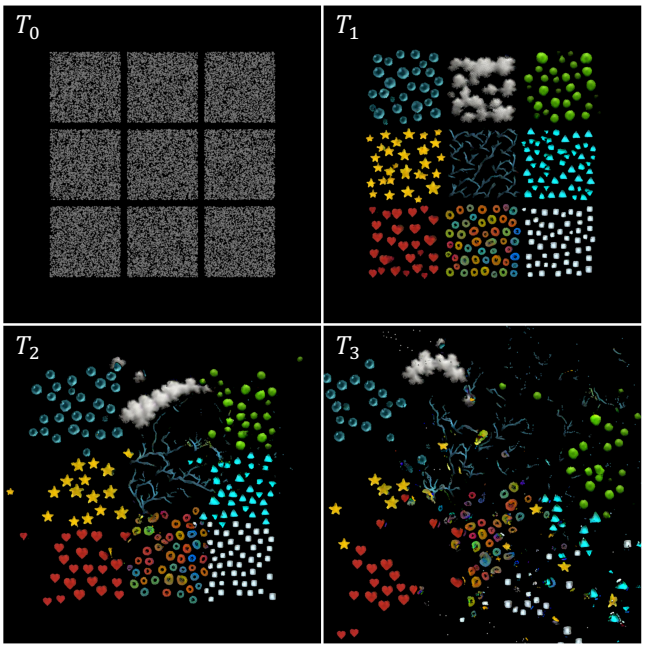


Fig. 14. Interaction of multiple independently trained NPA models.

they may serve as a distributed memory that helps maintain the morphology over long periods.

Finally, Figure 14 demonstrates that multiple independently trained NPA "species" can be composed within the same simulation. Each particle follows its own learned rule, and as groups move and interpenetrate they become part of one another's neighborhoods and therefore interact, despite never being co-trained. We observe a range of qualitative outcomes—from near-independence to cooperation and disruption—highlighting NPA as a candidate compact building block for multi-agent, self-organizing particle simulations.

5 Conclusion

We have presented Neural Particle Automata (NPA), a framework that generalizes NCA from fixed Eulerian grids to dynamic Lagrangian particle systems. By replacing grid-based convolutions with differentiable SPH operators and implementing them via custom CUDA kernels, we enable end-to-end training of self-organizing dynamics in continuous space. We demonstrated that NPA can perform a variety of self-organizing tasks, including morphogenesis modeling, particle-based texture synthesis, and self-classifying point clouds. We also showed that NPA model brings additional benefits such as perturbation robustness, controllable feature scale, generalization across particle resolutions, and support for multi-species interactions.

Limitations and future works. Several challenges emerged during our experiments. First, NPA cannot merge or split particles; consequently, when the target region is small, particles become denser and SPH operations slow down. This fixed particle count also limits the model's ability to capture fine geometric and texture details: regions that require higher resolution cannot recruit additional particles, while over-sampled regions cannot shed them. Second, NPA's gradient perceptions assume global Euclidean basis, limiting the model's generalization over rotations. Finally, the learning dynamics are sensitive to hyperparameters. These limitations suggest interesting future works, such as learning particle merging and splitting dynamics, rotation-invariant/equivariant architectures, and searching the optimal configurations.

Applications. Built upon mesh-free and local interactions, NPA have a wide range of applications. Because NPA directly process dynamic point data without meshing or conversion, the model can be used in tasks involving dynamic particles such as optimizing initial conditions for fluid simulations [Dehnen and Aly 2012], and point-cloud denoising. NPA's local perception mechanism can be easily extended beyond Euclidean geometry, such as texture synthesis on manifolds [Kim and Park 2025]. Additionally, As a trainable self-organizing system, NPA can learn a desired behavior of distributed dynamic systems, such as display systems made of drones or crowds.

Acknowledgments

This work was supported by Institute for Information & communications Technology Promotion(IITP) grant funded by the Korea government(MSIT) (No.00223446, Development of object-oriented synthetic data generation and evaluation methods)

References

Javier Bonet and T-SL Lok. 1999. Variational and momentum preservation aspects of smooth particle hydrodynamic formulations. *Computer Methods in applied mechanics and engineering* 180, 1-2 (1999), 97–115.

David S Broomhead and David Lowe. 1988. *Radial basis functions, multi-variable functional interpolation and adaptive networks.* Technical Report.

Scott Camazine, Jean-Louis Deneubourg, Nigel R Franks, James Sneyd, Guy Theraula, and Eric Bonabeau. 2020. Self-organization in biological systems. In *Self-Organization in Biological Systems*. Princeton university press.

Zhang Chen, Zhong Li, Liangchen Song, Lele Chen, Jingyi Yu, Junsong Yuan, and Yi Xu. 2023. Neurbf: A neural fields representation with adaptive radial basis functions. In *Proceedings of the IEEE/CVF International Conference on Computer Vision*. 4182–4194.

Mircea Cimpoi, Subhransu Maji, Iasonas Kokkinos, Sammy Mohamed, and Andrea Vedaldi. 2014. Describing textures in the wild. In *Proceedings of the IEEE conference on computer vision and pattern recognition*. 3606–3613.

Walter Dehnen and Hossam Aly. 2012. Improving convergence in smoothed particle hydrodynamics simulations without pairing instability. *Monthly Notices of the Royal Astronomical Society* 425, 2 (2012), 1068–1082.

Congyue Deng, Or Litany, Yueqi Duan, Adrien Poulenard, Andrea Tagliasacchi, and Leonidas J Guibas. 2021. Vector neurons: A general framework for so (3)-equivariant networks. In *Proceedings of the IEEE/CVF International Conference on Computer Vision*. 12200–12209.

Robert A Gingold and Joseph J Monaghan. 1977. Smoothed particle hydrodynamics: theory and application to non-spherical stars. *Monthly notices of the royal astronomical society* 181, 3 (1977), 375–389.

Prashant Goswami, Philipp Schlegel, Barbara Solenthaler, and Renato Pajarola. 2010. Interactive SPH Simulation and Rendering on the GPU.. In *Symposium on Computer Animation*. 55–64.

Daniele Grattarola, Lorenzo Livi, and Cesare Alippi. 2021. Learning graph cellular automata. *Advances in Neural Information Processing Systems* 34 (2021), 20983–20994.

Maxim Gumin. 2016. Wave Function Collapse. https://github.com/mxgmn/WaveFunctionCollapse. Accessed: Dec 3, 2025.

Rana Hanocka, Amir Hertz, Noa Fish, Raja Giryes, Shachar Fleishman, and Daniel Cohen-Or. 2019. Meshcnn: a network with an edge. *ACM Transactions on Graphics (ToG)* 38, 4 (2019), 1–12.

Andrew Hryniowski and Alexander Wong. 2019. Deeplabnet: End-to-end learning of deep radial basis networks with fully learnable basis functions. *arXiv preprint arXiv:1911.09257* (2019).

John Kalkhof, Camila González, and Anirban Mukhopadhyay. 2023. Med-nca: Robust and lightweight segmentation with neural cellular automata. In *International Conference on Information Processing in Medical Imaging*. Springer, 705–716.

Hyunsoo Kim and Jinah Park. 2025. Train Once, Generate Anywhere: Discretization Agnostic Neural Cellular Automata using SPH Method. In *Proceedings of the Special Interest Group on Computer Graphics and Interactive Techniques Conference Posters*. 1–2.

Nicholas Kolkin, Jason Salavon, and Gregory Shakhnarovich. 2019. Style transfer by relaxed optimal transport and self-similarity. In *Proceedings of the IEEE/CVF Conference on Computer Vision and Pattern Recognition*. 10051–10060.

Dan Koschier, Jan Bender, Barbara Solenthaler, and Matthias Teschner. 2022. A survey on SPH methods in computer graphics. In *Computer graphics forum*, Vol. 41. Wiley Online Library, 737–760.

Maria Larsson, Hodaka Yamaguchi, Ehsan Pajouheshgar, I-Chao Shen, Kenji Tojo, Chia-Ming Chang, Lars Hansson, Olof Broman, Takashi Ijiri, Ariel Shamir, Wenzel Jakob, and Takeo Igarashi. 2025. The Mokume Dataset and Inverse Modeling of Solid Wood Textures. *ACM Transactions on Graphics* 44, 4 (Aug. 2025), 18 pages. doi:10.1145/3730874

Yangyan Li, Rui Bu, Mingchao Sun, Wei Wu, Xinhan Di, and Baoquan Chen. 2018. Pointcnn: Convolution on x-transformed points. *Advances in neural information processing systems* 31 (2018).

Zhaowei Liu, Dong Yang, Yingjie Wang, Mingjie Lu, and Ranran Li. 2023. EGNN: Graph structure learning based on evolutionary computation helps more in graph neural networks. *Applied Soft Computing* 135 (2023), 110040.

Leon B Lucy. 1977. A numerical approach to the testing of the fission hypothesis. *Astronomical Journal, vol. 82, Dec. 1977, p. 1013-1024.* 82 (1977), 1013–1024.

Arman Maesumi, Tanish Makadia, Thibault Groueix, Vladimir G Kim, Daniel Ritchie, and Noam Aigerman. 2025. PoissonNet: A Local-Global Approach for Learning on Surfaces. *arXiv preprint arXiv:2510.14146* (2025).

Leland McInnes, John Healy, Nathaniel Saul, and Lukas Grossberger. 2018. UMAP: Uniform Manifold Approximation and Projection. *The Journal of Open Source Software* 3, 29 (2018), 861.

Paul Merrell and Dinesh Manocha. 2010. Model synthesis: A general procedural modeling algorithm. *IEEE transactions on visualization and computer graphics* 17, 6 (2010), 715–728.

Ben Mildenhall, Pratul P Srinivasan, Matthew Tancik, Jonathan T Barron, Ravi Ramamoorthi, and Ren Ng. 2021. Nerf: Representing scenes as neural radiance fields for view synthesis. *Commun. ACM* 65, 1 (2021), 99–106.

Davoud Mirzaei, Robert Schaback, and Mehdi Dehghan. 2012. On generalized moving least squares and diffuse derivatives. *IMA J. Numer. Anal.* 32, 3 (2012), 983–1000.

Tom Mohr. 2022. Particle Life Simulator. http://particle-life.com/. Open-source Java simulation of emergent particle life, using parallel processing and space partitioning; includes GitHub, YouTube, and Discord components.

Alexander Mordvintsev, Eyvind Niklasson, and Ettore Randazzo. 2022a. Particle Lenia and the energy-based formulation. https://google-research.github.io/self-organising-systems/particle-lenia/. Accessed: 2025-09-08.

Alexander Mordvintsev, Ettore Randazzo, and Craig Fouts. 2022b. Growing isotropic neural cellular automata. In *Artificial Life Conference Proceedings 34*, Vol. 2022. MIT Press One Rogers Street, Cambridge, MA 02142-1209, USA journals-info …, 65.

Alexander Mordvintsev, Ettore Randazzo, and Eyvind Niklasson. 2021. Differentiable programming of reaction-diffusion patterns. In *Artificial Life Conference Proceedings 33*, Vol. 2021. MIT Press One Rogers Street, Cambridge, MA 02142-1209, USA journals-info …, 28.

Alexander Mordvintsev, Ettore Randazzo, Eyvind Niklasson, and Michael Levin. 2020. Growing neural cellular automata. *Distill* 5, 2 (2020), e23.

Matthias Müller, David Charypar, and Markus Gross. 2003. Particle-based fluid simulation for interactive applications. In *Proceedings of the 2003 ACM SIGGRAPH/Eurographics symposium on Computer animation*. Citeseer, 154–159.

Eyvind Niklasson, Alexander Mordvintsev, Ettore Randazzo, and Michael Levin. 2021. Self-organising textures. *Distill* 6, 2 (2021), e00027–003.

Ehsan Pajouheshgar, Yitao Xu, Ali Abbasi, Alexander Mordvintsev, Wenzel Jakob, and Sabine Süsstrunk. 2025. Neural Cellular Automata: From Cells to Pixels. *arXiv preprint arXiv:2506.22899* (2025).

Ehsan Pajouheshgar, Yitao Xu, Alexander Mordvintsev, Eyvind Niklasson, Tong Zhang, and Sabine Süsstrunk. 2024b. Mesh Neural Cellular Automata. *ACM Trans. Graph.* (2024). doi:10.1145/3658127

Ehsan Pajouheshgar, Yitao Xu, and Sabine Süsstrunk. 2024a. NoiseNCA: Noisy Seed Improves Spatio-Temporal Continuity of Neural Cellular Automata *(Artificial Life Conference Proceedings, Vol. ALIFE 2024: Proceedings of the 2024 Artificial Life Conference)*. 57. arXiv:https://direct.mit.edu/isal/proceedings-pdf/isal2024/36/57/2461193/isal_a_00785.pdf doi:10.1162/isal_a_00785

Ehsan Pajouheshgar, Yitao Xu, Tong Zhang, and Sabine Süsstrunk. 2023. DyNCA: Real-time Dynamic Texture Synthesis Using Neural Cellular Automata. In *Proceedings of the IEEE/CVF Conference on Computer Vision and Pattern Recognition*. 20742–20751.

Charles R Qi, Hao Su, Kaichun Mo, and Leonidas J Guibas. 2017a. Pointnet: Deep learning on point sets for 3d classification and segmentation. In *Proceedings of the IEEE conference on computer vision and pattern recognition*. 652–660.

Charles Ruizhongtai Qi, Li Yi, Hao Su, and Leonidas J Guibas. 2017b. Pointnet++: Deep hierarchical feature learning on point sets in a metric space. *Advances in neural information processing systems* 30 (2017).

Ettore Randazzo, Alexander Mordvintsev, Eyvind Niklasson, Michael Levin, and Sam Greydanus. 2020. Self-classifying mnist digits. *Distill* 5, 8 (2020), e00027–002.

Craig W Reynolds. 1987. Flocks, herds and schools: A distributed behavioral model. In *Proceedings of the 14th annual conference on Computer graphics and interactive techniques*. 25–34.

Connor Schenck and Dieter Fox. 2018. Spnets: Differentiable fluid dynamics for deep neural networks. In *Conference on Robot Learning*. PMLR, 317–335.

Nicholas Sharp, Souhaib Attaiki, Keenan Crane, and Maks Ovsjanikov. 2022. Diffusionnet: Discretization agnostic learning on surfaces. *ACM Transactions on Graphics (TOG)* 41, 3 (2022), 1–16.

Karen Simonyan and Andrew Zisserman. 2015. Very Deep Convolutional Networks for Large-Scale Image Recognition. In *3rd International Conference on Learning Representations, ICLR 2015, San Diego, CA, USA, May 7-9, 2015, Conference Track Proceedings*, Yoshua Bengio and Yann LeCun (Eds.). http://arxiv.org/abs/1409.1556

Hugues Thomas, Charles R Qi, Jean-Emmanuel Deschaud, Beatriz Marcotegui, François Goulette, and Leonidas J Guibas. 2019. Kpconv: Flexible and deformable convolution for point clouds. In *Proceedings of the IEEE/CVF international conference on computer vision*. 6411–6420.

Artur P Toshev, Harish Ramachandran, Jonas A Erbesdobler, Gianluca Galletti, Johannes Brandstetter, and Nikolaus A Adams. 2024. Jax-sph: A differentiable smoothed particle hydrodynamics framework. *arXiv preprint arXiv:2403.04750* (2024).

AM Turing. 1952. The Chemical Basis of Morphogenesis. *Philosophical Transactions of the Royal Society of London Series B* 237, 641 (1952), 37–72.

Ashish Vaswani, Noam Shazeer, Niki Parmar, Jakob Uszkoreit, Llion Jones, Aidan N Gomez, Łukasz Kaiser, and Illia Polosukhin. 2017. Attention is all you need. *Advances in neural information processing systems* 30 (2017).

Jeffrey Ventrella. 2016. Clusters. https://ventrella.com/Clusters/intro.html. Accessed: 2025-09-08.

John von Neumann. 1966. Theory of self-reproducing automata. *Math. Comp.* 21 (1966), 745.

Ruben Wiersma, Ahmad Nasikun, Elmar Eisemann, and Klaus Hildebrandt. 2022. Deltaconv: anisotropic operators for geometric deep learning on point clouds. *ACM Transactions on Graphics (TOG)* 41, 4 (2022), 1–10.

Rene Winchenbach and Nils Thuerey. 2025. diffSPH: Differentiable Smoothed Particle Hydrodynamics for Adjoint Optimization and Machine Learning. *arXiv preprint arXiv:2507.21684* (2025).

Andrew Witkin and Michael Kass. 1991. Reaction-diffusion textures. In *Proceedings of the 18th annual conference on Computer graphics and interactive techniques*. 299–308.

Wenxuan Wu, Zhongang Qi, and Li Fuxin. 2019. Pointconv: Deep convolutional networks on 3d point clouds. In *Proceedings of the IEEE/CVF Conference on computer vision and pattern recognition*. 9621–9630.

Vickie Ye, Ruilong Li, Justin Kerr, Matias Turkulainen, Brent Yi, Zhuoyang Pan, Otto Seiskari, Jianbo Ye, Jeffrey Hu, Matthew Tancik, and Angjoo Kanazawa. 2025. gsplat: An open-source library for Gaussian splatting. *Journal of Machine Learning Research* 26, 34 (2025), 1–17.

Hengshuang Zhao, Li Jiang, Jiaya Jia, Philip HS Torr, and Vladlen Koltun. 2021. Point transformer. In *Proceedings of the IEEE/CVF international conference on computer vision*. 16259–16268.

A Backward Derivations of SPH Operators

Notation. We denote reverse-mode (incoming) gradients by $\bar{y} := \frac{\partial \mathcal{L}}{\partial y}$. Particle positions are $\mathbf{x}_i \in \mathbb{R}^D$, densities are $\rho_i \in \mathbb{R}$, and states are $\mathbf{S}_i \in \mathbb{R}^C$. We define pairwise offsets $\mathbf{r}_{ij} := \mathbf{x}_i - \mathbf{x}_j$, distance $d_{ij} := \|\mathbf{r}_{ij}\|$, and neighborhood $\mathcal{N}(i) := \{j \mid d_{ij} < \epsilon\}$. All kernels and their derivatives are identically zero for $d_{ij} \geq \epsilon$. At $d_{ij} = 0$, direction-dependent terms are set to zero in practice to avoid singularities.

A.1 Kernels

We use the Poly6 kernel W_ϵ and the Spiky gradient kernel W_ϵ^∇:

$$\begin{aligned} W_\epsilon(\mathbf{r}) &= Z_\epsilon \left(\epsilon^2 - \|\mathbf{r}\|^2\right)^3, \\ W_\epsilon^\nabla(\mathbf{r}) &= Z_\epsilon^\nabla \left(\epsilon - \|\mathbf{r}\|\right)^2 \frac{\mathbf{r}}{\|\mathbf{r}\|}. \end{aligned} \tag{9}$$

where Z_ϵ denotes the Poly6 normalization constant and Z_ϵ^∇ denotes the Spiky-gradient normalization constant. In 2D, we use $Z_\epsilon = \frac{4}{\pi\epsilon^8}$ and $Z_\epsilon^\nabla = \frac{10}{\pi\epsilon^5}$, while in 3D we use $Z_\epsilon = \frac{315}{64\pi\epsilon^9}$ and $Z_\epsilon^\nabla = \frac{15}{\pi\epsilon^6}$.

The backward pass requires (i) the spatial derivative of W_ϵ, and (ii) the Jacobian of W_ϵ^∇. For $0 < d = \|\mathbf{r}\| < \epsilon$, the Poly6 gradient is

$$\nabla_\mathbf{r} W_\epsilon(\mathbf{r}) = -6 Z_\epsilon \left(\epsilon^2 - \|\mathbf{r}\|^2\right)^2 \mathbf{r}. \tag{10}$$

Let $\mathbf{H}_\epsilon(\mathbf{r}) := \frac{\partial W_\epsilon^\nabla}{\partial \mathbf{r}} \in \mathbb{R}^{D\times D}$ be the Jacobian of the Spiky gradient kernel. For $0 < d = \|\mathbf{r}\| < \epsilon$,

$$\mathbf{H}_\epsilon(\mathbf{r}) = 3 Z_\epsilon^\nabla \left(\frac{(\epsilon - d)^2}{d} \mathbf{I} - \frac{\epsilon^2 - d^2}{d^3} \mathbf{r}\mathbf{r}^\top \right), \tag{11}$$

where $\mathbf{I}$ is the $D \times D$ identity matrix.

A.2 Backward Derivations

(1) Density.

$$\rho_i = \sum_{j \in \mathcal{N}(i)} m_j \, W_\epsilon(\mathbf{r}_{ij}). \tag{12}$$

The position gradient is

$$\frac{\partial \mathcal{L}}{\partial \mathbf{x}_i} = \sum_{j \in \mathcal{N}(i)} \left(m_j \, \bar{\rho}_i + m_i \, \bar{\rho}_j \right) \, \nabla_\mathbf{r} W_\epsilon(\mathbf{r}_{ij}). \tag{13}$$

(2) Smoothing (blur).

$$\tilde{\mathbf{S}}_i = \sum_{j \in \mathcal{N}(i)} \frac{m_j}{\rho_j} \, \mathbf{S}_j \, W_\epsilon(\mathbf{r}_{ij}). \tag{14}$$

The gradients w.r.t. $\mathbf{S}_i$ and ρ_i are

$$\frac{\partial \mathcal{L}}{\partial \mathbf{S}_i} = \frac{m_i}{\rho_i} \sum_{j \in \mathcal{N}(i)} W_\epsilon(\mathbf{r}_{ij}) \, \bar{\tilde{\mathbf{S}}}_j, \tag{15}$$

$$\frac{\partial \mathcal{L}}{\partial \rho_i} = -\frac{m_i}{\rho_i^2} \sum_{j \in \mathcal{N}(i)} W_\epsilon(\mathbf{r}_{ij}) \, \bar{\tilde{\mathbf{S}}}_j^\top \mathbf{S}_i. \tag{16}$$

The position gradient is

$$\frac{\partial \mathcal{L}}{\partial \mathbf{x}_i} = \sum_{j \in \mathcal{N}(i)} \left[\bar{\tilde{\mathbf{S}}}_i^\top \left(\frac{m_j}{\rho_j} \mathbf{S}_j \right) + \bar{\tilde{\mathbf{S}}}_j^\top \left(\frac{m_i}{\rho_i} \mathbf{S}_i \right) \right] \nabla_\mathbf{r} W_\epsilon(\mathbf{r}_{ij}). \tag{17}$$

(3) Gradient (0-th order difference form). We write the operator as

$$\mathbf{G}_i := \nabla^0 \mathbf{S}_i = \sum_{j \in \mathcal{N}(i)} \frac{m_j}{\rho_j} (\mathbf{S}_i - \mathbf{S}_j) \otimes W_\epsilon^\nabla(\mathbf{r}_{ij}) \in \mathbb{R}^{C \times D}. \tag{18}$$

The gradient w.r.t. $\mathbf{S}_i$ is

$$\frac{\partial \mathcal{L}}{\partial \mathbf{S}_i} = \sum_{j \in \mathcal{N}(i)} \left(\frac{m_j}{\rho_j} \bar{\mathbf{G}}_i + \frac{m_i}{\rho_i} \bar{\mathbf{G}}_j \right) W_\epsilon^\nabla(\mathbf{r}_{ij}), \tag{19}$$

where the matrix–vector multiplication produces a C-vector. The density gradient is

$$\frac{\partial \mathcal{L}}{\partial \rho_i} = -\frac{m_i}{\rho_i^2} \sum_{j \in \mathcal{N}(i)} (\mathbf{S}_i - \mathbf{S}_j)^\top \bar{\mathbf{G}}_j \, W_\epsilon^\nabla(\mathbf{r}_{ij}). \tag{20}$$

The position gradient is obtained by backpropagating through W_ϵ^∇:

$$\frac{\partial \mathcal{L}}{\partial \mathbf{x}_i} = \sum_{j \in \mathcal{N}(i)} \mathbf{H}_\epsilon(\mathbf{r}_{ij})^\top \left(\frac{m_j}{\rho_j} \bar{\mathbf{G}}_i + \frac{m_i}{\rho_i} \bar{\mathbf{G}}_j \right)^\top (\mathbf{S}_i - \mathbf{S}_j). \tag{21}$$

(4) Density gradient.

$$\nabla \rho_i = \sum_{j \in \mathcal{N}(i)} m_j \, W_\epsilon^\nabla(\mathbf{r}_{ji}) \in \mathbb{R}^D. \tag{22}$$

Let $\bar{\mathbf{g}}_i := \frac{\partial \mathcal{L}}{\partial (\nabla \rho_i)} \in \mathbb{R}^D$. Then

$$\frac{\partial \mathcal{L}}{\partial \mathbf{x}_i} = \sum_{j \in \mathcal{N}(i)} \mathbf{H}_\epsilon(\mathbf{r}_{ij})^\top \left(m_i \, \bar{\mathbf{g}}_j - m_j \, \bar{\mathbf{g}}_i \right). \tag{23}$$

(5) Moment matrix.

$$\mathbf{M}_i = \sum_{j \in \mathcal{N}(i)} \frac{m_j}{\rho_j} \, \mathbf{r}_{ji} \, W_\epsilon^\nabla(\mathbf{r}_{ji})^\top \in \mathbb{R}^{D \times D}. \tag{24}$$

Let $\bar{\mathbf{M}}_i := \frac{\partial \mathcal{L}}{\partial \mathbf{M}_i} \in \mathbb{R}^{D \times D}$ and $\langle \mathbf{A}, \mathbf{B} \rangle_F := \mathrm{tr}(\mathbf{A}^\top \mathbf{B})$. The density gradient is

$$\frac{\partial \mathcal{L}}{\partial \rho_i} = -\frac{m_i}{\rho_i^2} \sum_{j \in \mathcal{N}(i)} \left\langle \bar{\mathbf{M}}_j, \; \mathbf{r}_{ij} \, W_\epsilon^\nabla(\mathbf{r}_{ij})^\top \right\rangle_F. \tag{25}$$

For the position gradient, define the pairwise coefficient matrix

$$\mathbf{C}_{ij} := \frac{m_j}{\rho_j} \bar{\mathbf{M}}_i + \frac{m_i}{\rho_i} \bar{\mathbf{M}}_j \in \mathbb{R}^{D \times D}. \tag{26}$$

Then

$$\frac{\partial \mathcal{L}}{\partial \mathbf{x}_i} = \sum_{j \in \mathcal{N}(i)} \left[\mathbf{C}_{ij} \, W_\epsilon^\nabla(\mathbf{r}_{ij}) + \mathbf{H}_\epsilon(\mathbf{r}_{ij})^\top \left(\mathbf{C}_{ij}^\top \mathbf{r}_{ij} \right) \right]. \tag{27}$$

B CUDA Implementation of SPH Operators

We implement all forward SPH operators using a uniform hash grid and custom CUDA kernels. Rather than storing an explicit adjacency list (which is variable-sized and expensive for dynamic particle sets), we build a compact spatial index that lets each particle enumerate candidate neighbors by scanning the small set of adjacent grid cells and filtering by the true support radius.

We first *bin* particles into grid cells of size equal to the SPH support radius. This binning produces a *cell-contiguous* layout in memory: particles belonging to the same cell occupy a single contiguous interval. Forward kernels then iterate over the 3^D neighbor cells (e.g., 3×3 in 2D, $3 \times 3 \times 3$ in 3D), load candidate particles from those cell intervals, and accumulate operator-specific contributions.

We provide implementations of two different approaches for parallelizing the computation and neighborhood traversal:

- **Particle-Centric (Morton hashing):** One CUDA thread per particle; neighborhoods are streamed directly from global memory. We use Morton (Z-order) hashing so spatially nearby cells tend to be close in memory after binning, improving cache locality when each thread independently scans the 3^D neighboring cells.
- **Grid-Centric (Row-major hashing + shared memory):** We assign CUDA blocks to grid cells (splitting high-occupancy cells across multiple blocks as needed). We use row-major hashing to preserve contiguity along the x-dimension, enabling threads to cooperatively load neighbor particle data from global memory into shared memory as *consecutive* contiguous spans, then reuse the staged data across all particles in the block.

B.1 Hash-Grid Binning and Data Structures

For simplicity we assume all particles have an equal mass that does not change over time. Given an input batch of particles ($\mathbf{x} \in \mathbb{R}^{B \times N \times D}, \mathbf{S} \in \mathbb{R}^{B \times N \times C}$), where B is the batch size and N is the number of particles in a batch, we construct:

- **Cell counts** `cellCount`$[b, h]$: number of particles that fall into cell h in batch b.
- **Cell offsets** `cellOffset`$[b, h]$: cumulative sum over counts, giving the start index of particles for cell h in the binned particle arrays.
- **Permutation** `perm`$[b, i]$: the destination index of particle b, i in the binned layout.
- **Binned arrays** `xBin`, `SBin`: particle positions and features permuted such that each cell occupies one contiguous range ordered with the cell index.

In the grid-centric variant, we additionally build:

- **Block descriptors** `BlockInfo`: a compact list that maps each CUDA block to a particular cell (and optionally an offset range within that cell for load balancing when cells are very full).

B.2 Particle-Centric Approach

We assign one CUDA thread per particle in the binned arrays. Each thread computes the output of the chosen SPH operator for its particle by iterating over neighbor candidates.

Neighborhood traversal. For a particle i a CUDA thread:

(1) Computes i's cell and its hash h.
(2) Enumerates the 3^D adjacent cells around h.
(3) For each neighbor cell, obtains the particle range [`cellOffset`$[h_n]$, `cellOffset`$[h_n + 1]$).
(4) Iterates through that contiguous range in global memory and applies a radius check ($\|\mathbf{x}_j - \mathbf{x}_i\| < \epsilon$) before accumulating operator contributions.

Core design points.

- **No shared memory.** This keeps the kernel simple and avoids block-level synchronization.

- **Morton hashing for cache efficiency.** Since neighbor scanning reads global memory directly, we rely on the binned Morton layout to improve cache hit rates and reduce memory divergence.
- **Stable work pattern.** Each particle does the same conceptual work (scan neighbor cells, then radius filter), with variable neighbor counts handled naturally by loops.

B.3 Shared-Memory Forward Kernel (GridBased)

We assign each CUDA block to a specific grid cell. If a cell contains many particles, we split it into multiple blocks to improve load balancing across blocks. We store the mapping between blocks and cells in `BlockInfo` data structure.

Within a CUDA block:

- We first cooperatively load the block's *local particles* (those in the assigned cell chunk and any required attributes such as state or density) into shared memory.
- We then iterate over the neighbor cells, where all threads in the block perform cooperative, coalesced reads of neighbor particle data into shared memory.

The grid-centric kernel is designed so that neighbor particles are fetched in a small number of *contiguous* global-memory spans:

- **In 2D:** the block reads 3 consecutive spans corresponding to the *top*, *middle*, and *bottom* neighbor rows. Each row span covers the 3 adjacent x-cells, so each row can often be fetched as one contiguous interval.
- **In 3D:** the block reads 9 consecutive spans corresponding to all $(\Delta y, \Delta z) \in \{-1, 0, 1\}^2$ neighbor rows. Again, each span covers the 3 adjacent x-cells.

We use **row-major hashing** in this variant specifically so that, for a fixed neighbor row, the three x-neighbor cells map to consecutive cell hashes and therefore to a contiguous particle interval after binning.

Neighbor rows may contain more particles than the available shared memory. We therefore process each neighbor row in *chunks*:

- Threads cooperatively load a fixed-size chunk (STRIDE) of neighbor particle data into shared memory.
- All threads then compute interactions between their assigned local particles and the staged neighbor chunk.
- We repeat until the entire neighbor span has been processed.

This preserves coalesced loads, maximizes reuse of staged neighbor data, and keeps shared memory bounded.

Core design points.

- **Reuse local data.** Local particles stay in shared memory while the kernel streams over neighbor chunks, reducing repeated global reads.
- **Coalesced global access.** Neighbor particles are read as contiguous spans (3 spans in 2D, 9 spans in 3D), which reduces memory transaction overhead relative to per-thread random access.
- **Robust to variable cell occupancy.** Cells with many particles are split across multiple blocks and empty cells generate no blocks.

B.4 Comparison with Prior Work

Our implementation shares architectural similarities with the work of Goswami et al. [2010], whose method can be viewed as a hybrid of our particle-centric and grid-centric approaches. Like our particle-centric variant, each of their threads is responsible for a single particle and they employ Morton (Z-order) hashing for spatial indexing. At the same time, threads cooperatively load neighboring particles into shared memory and a compact block descriptor (analogous to our `BlockInfo`) assigns thread blocks to spatial regions, which parallels our grid-centric design.

Our grid-centric approach differs in two key respects. First, we use row-major hashing so that, for a given neighbor row, the three adjacent x-cells map to consecutive cell hashes and can therefore be fetched as a single contiguous span in a coalesced read. This is particularly beneficial in our setting, where each particle carries a C-dimensional feature state, substantially more data per particle than the position-and-velocity attributes typical of fluid simulations such as theirs. Second, our strided loop design allows each thread to process multiple local and neighbor particles, decoupling the thread count from the cell occupancy and improving utilization when cells vary in size.

Goswami et al. [2010] additionally employ two optimization techniques: (i) pre-computing SPH kernel values for discretized distances and storing them in CUDA constant memory as lookup tables, and (ii) an interleaved load-compute pattern in which each thread issues global memory loads for the next batch of neighbor particles while simultaneously computing interactions against the previously loaded batch, thereby overlapping memory latency with arithmetic work.

We evaluated both ideas in our implementation. The kernel lookup table degrades performance on modern hardware because threads within a warp evaluate the SPH kernel at different distances, producing divergent addresses into the constant memory array. Constant memory is optimized for uniform (broadcast) access; under divergent access the reads serialize, making the lookup slower than directly computing our smoothing and spiky kernels, which require only a few floating-point operations each. The interleaved load-compute pattern requires double-buffering the neighbor data in shared memory, roughly doubling the shared memory footprint of the neighbor-side buffers. In our experiments this increased register pressure and reduced occupancy, yielding a slight net slowdown for the particle counts and neighborhood densities we tested. The technique may nevertheless prove beneficial at larger scales with denser neighborhoods, where the compute-to-load ratio per chunk is high enough to fully hide the memory latency.

C Evaluations

We provide (i) a qualitative comparison to GrowingNCA on a shared morphogenesis task, (ii) a forward-pass scaling benchmark comparing our CUDA SPH perception against a convolutional NCA baseline, and (iii) an ablation study isolating key design choices in SPH perception and training stabilization, as well as the choice of perception radius ϵ. All benchmarks are run on an NVIDIA GeForce RTX 4090 GPU.

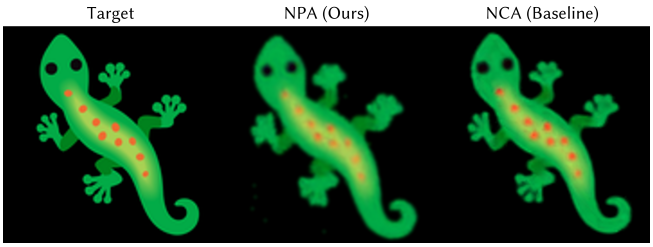


Fig. 15. Qualitative comparison on morphogenesis: GrowingNCA (grid) vs. NPA (particles) for the same target and similar active-cell/particle budget.

C.1 Qualitative Comparison with GrowingNCA

As there is no established baseline for *trainable* self-organizing *particle* dynamics, we compare NPA to the most closely related neural-automata baseline: GrowingNCA. We evaluate both methods on the same task of growing a target morphology from a simple seed. NPA starts with a fixed set of particles present from the beginning, whereas GrowingNCA starts from a single live cell and grows a variable number of active cells over time.

To make the comparison as fair as possible, we choose the GrowingNCA grid resolution so that the final number of active cells is comparable to our particle count (N=4096). For the lizard target, this corresponds to approximately a 120×120 grid. Both models use the same training setup (batch size, $[T_{\min}, T_{\max}]$, pool size, channel count, and MLP width). We use the standard GrowingNCA learning rate of 10^{-3}, while NPA uses $5{\times}10^{-4}$. On this setup, GrowingNCA training takes ∼14 minutes per 10k iterations and uses 11.4 GB of GPU memory, while NPA takes ∼29 minutes per 10k iterations and uses 6.2 GB. Figure 15 shows that both methods reach comparable visual quality; NPA is slower per iteration but notably more memory efficient in this regime.

C.2 Performance Comparison with NCA

We next compare inference-time scaling by measuring the wall-clock time and reserved GPU memory for a *single* forward update step. For NPA, we uniformly distribute N particles in $[-1.6, 1.6]^2$ and set $\epsilon \approx 0.2\sqrt{1024/N}$ to keep the expected neighbor count approximately constant (about 13 neighbors per particle). For NCA, we vary the grid size so that the number of cells matches N, noting that the convolutional perception radius remains fixed (a 3×3 neighborhood, i.e., 9 neighbors).

Figure 16 shows that both approaches exhibit a constant-time regime at small sizes (GPU under-utilization) and transition to roughly linear scaling once the GPU is saturated. NPA has a higher constant factor in step time, consistent with (i) a slightly larger neighborhood (13 vs. 9) and (ii) the higher arithmetic intensity of SPH perception compared to a fixed 3×3 convolution.

C.3 Ablation Study

We ablate three key components used in our SPH-based perception and training stabilization: (i) stopping gradients through particle positions, (ii) logarithmic normalization of vector-valued perception terms, and (iii) removing directional perception (state gradients and density gradient). We run all ablations on the 2D morphogenesis setting (lizard target) and report the training loss over iterations.

As shown in Figure 17, removing directional perception prevents effective learning. Both stabilization choices still allow learning but are substantially less stable: without stopping gradients through positions, training diverges early; without log normalization, training is initially stable but becomes brittle after a pool reset (iteration 10k), often leading to divergence. Notably, both unstable variants also plateau at higher loss than our full model throughout training, indicating reduced learning capacity in addition to poorer stability.

We perform a sweep over the SPH support radius ϵ to study its impact on both accuracy and runtime. Figure 18 reports PointMNIST classification error and training time when varying ϵ over a 0.5×–2× range. Smaller ϵ yields noisier perception due to too few neighbors, degrading accuracy, while larger ϵ increases the average neighbor count and therefore slows training (runtime scales approximately linearly with the number of neighbors). We choose ϵ in the main experiments based on this accuracy-runtime trade-off.

D Online Interactive Demo

To make the learned dynamics tangible in a graphics setting, we provide an online, browser-based interactive demo that runs trained NPA models in real time and allows direct user interaction with the particle system: **https://selforg-npa.github.io/**. The demo comes in two variants—a *Growing Demo* (targets are emoji-like shapes) and a *Texture Demo* (targets are RGBA textures, sourced from DTD [Cimpoi et al. 2014] or generated using a text-to-image generator.). Both variants share the same graphics shader; they differ only in the initialization and the loaded network weights.

Our implementation is built with *SwissGL*, a lightweight wrapper over the WebGL2 API that streamlines the management of GLSL shaders and GPU buffers. We represent the particle set as floating-point textures: each particle stores its multi-channel state and its position, and NPA inference is executed by repeatedly applying a small set of fragment shaders that (i) build an indexing structure for neighborhood queries, (ii) evaluate SPH-style perception and the learned NPA update, and (iii) render particles via Gaussian splatting.

A central challenge for real-time NPA inference in the browser is neighborhood aggregation on a dynamic particle set. To avoid all-pairs interactions, we build a shader-friendly spatial index directly in SwissGL. Particles are sorted by a spatial key using the bitonic sort algorithm. Since particles typically move only slightly per update, we apply a short *maintenance* sort after each step rather than a full re-sorting, which substantially improves performance. After sorting, we compute coarse per-block bounding boxes and use bounding-box intersection tests to identify candidate neighboring blocks, yielding a compact set of blocks to scan during SPH accumulation.

The core NPA computation is implemented as two shaders. First, a density pass estimates (inverse) local density for each particle using the same neighborhood scan. Second, the update pass accumulates SPH perception features (e.g., smoothing and gradients) over the candidate neighborhood and applies the learned adaptation MLP in a fused manner directly within the same shader, with network weights stored as textures.

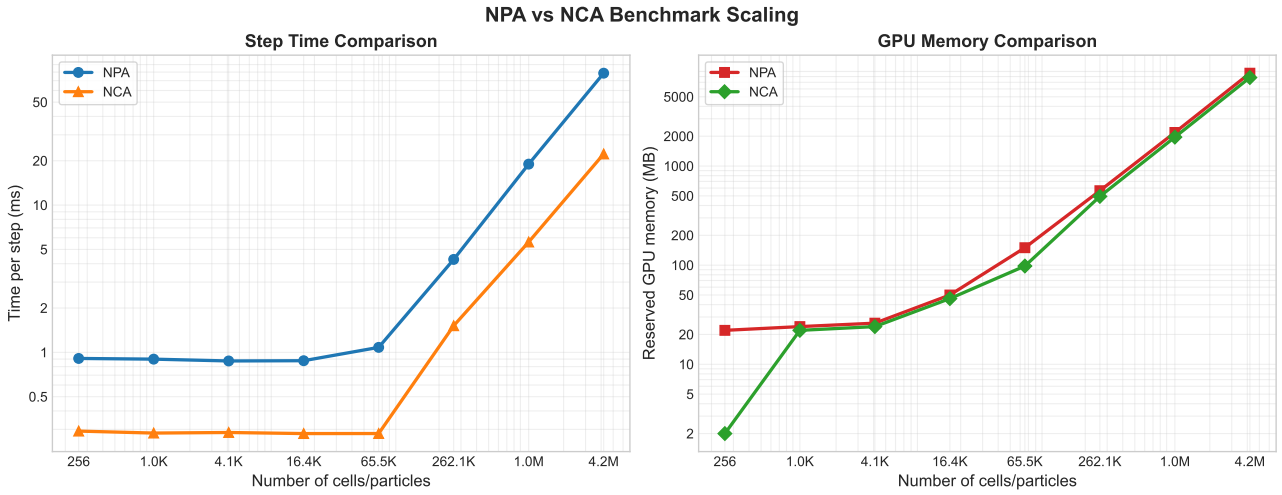


Fig. 16. Forward-step scaling on RTX 4090: step time (left) and reserved GPU memory (right) vs. number of particles/cells for NPA and convolutional NCA.



Fig. 17. Ablation study on SPH perception: removing gradients prevents learning; removing stop-gradient or log normalization reduces stability and can cause divergence.

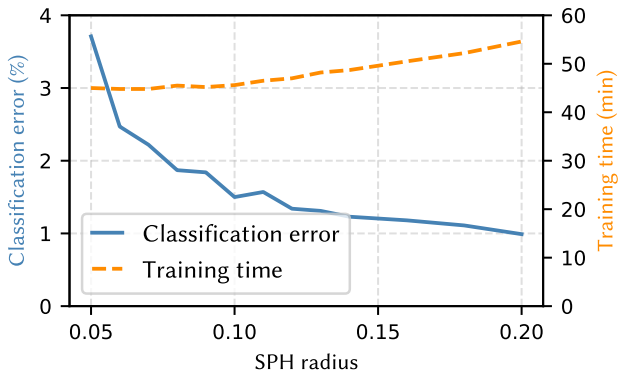


Fig. 18. Classification error (left axis) and training time (right axis) vs. SPH radius (ϵ) in PointMNIST classification.

For visualization, each particle is rendered as a Gaussian splat or a circle into an image buffer. We use a test-time compositing rule $d \cdot (1 - s_a) + s$ where d is the current buffer value, s is the fragment-emitted color and s_a its alpha. This blending prevents color saturation when many splats overlap and produces stable, readable renderings during interaction. The demo also includes a *trace* option that highlights a sparse subset of particles by rendering them with larger splats, making long-term trajectories and persistent flows easier to observe. The trace mode also shows the the perception radius of the traced particles, ϵ, as a red circle around them, as shown in Figure 19.

The UI exposes interactive controls commonly needed to explore NPA behavior: support radius ϵ, simulation speed (steps per frame), splat radius, and particle count. Particle count is restricted to powers of two to match the bitonic sort implementation. We also provide brush-based perturbations to demonstrate robustness and regeneration under user intervention: (i) zeroing particle states in a region, (ii) pushing particles along a stroke (cut/scissor-like), and (iii) pulling particles toward a point (magnet-like). These tools let users directly probe the locality, stability, and regenerative properties of the learned particle dynamics in a way that complements the offline figures and videos.

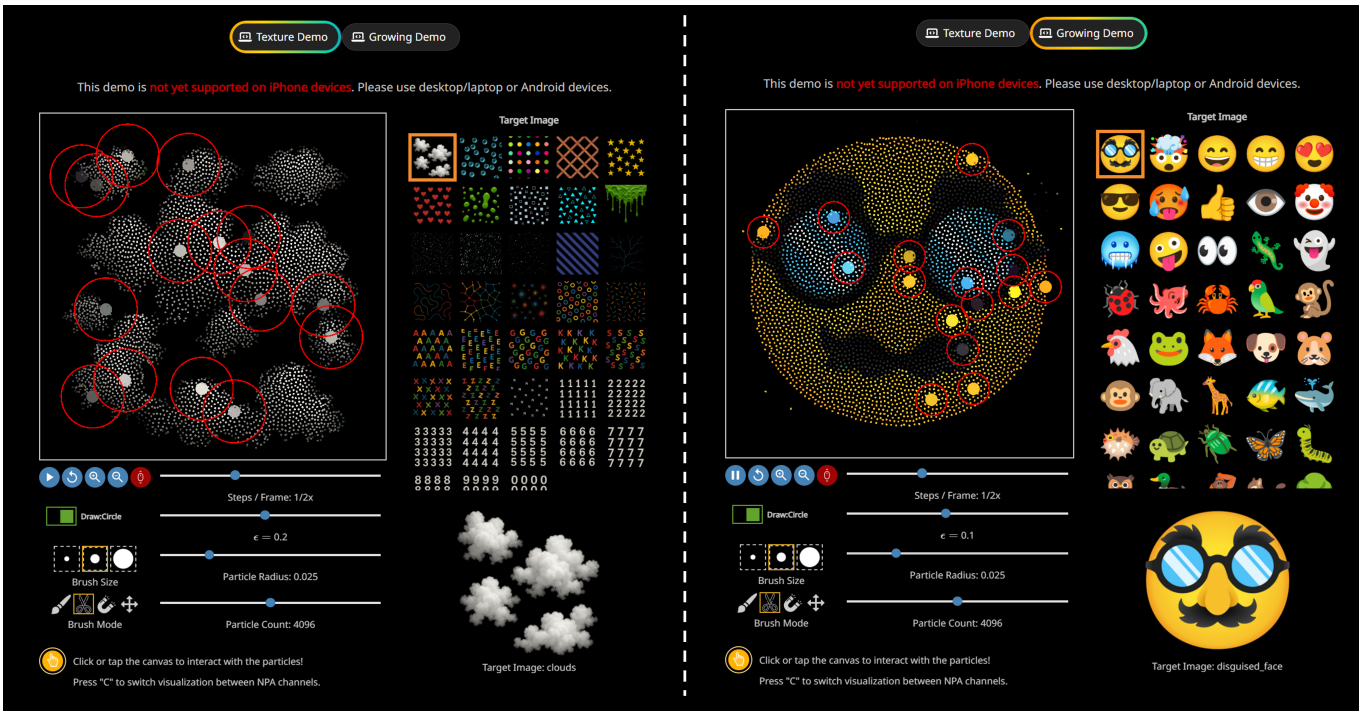


Fig. 19. Snapshot of the interactive web demo. Activating trace mode highlights a random set of particles as well as their perception range.